ACSNANO

www.acsnano.org

ARTICLE

The Bulk van der Waals Layered Magnet CrSBr is a Quasi-1D Material

Julian Klein,* Benjamin Pingault, Matthias Florian, Marie-Christin Heißenbüttel, Alexander Steinhoff, Zhigang Song, Kierstin Torres, Florian Dirnberger, Jonathan B. Curtis, Mads Weile, Aubrey Penn, Thorsten Deilmann, Rami Dana, Rezlind Bushati, Jiamin Quan, Jan Luxa, Zdeněk Sofer, Andrea Alù, Vinod M. Menon, Ursula Wurstbauer, Michael Rohlfing, Prineha Narang,* Marko Lončar,* and Frances M. Ross*

Cite This: *ACS Nano* 2023, 17, 5316−5328

Read Online

ACCESS | Metrics & More | Article Recommendations | Supporting Information

ABSTRACT: **Correlated quantum phenomena in one-dimensional (1D) systems that exhibit competing electronic and magnetic order are of strong interest for the study of fundamental interactions and excitations, such as Tomonaga−Luttinger liquids and topological orders and defects with properties completely different from the quasiparticles expected in their higher-dimensional counterparts. However, clean 1D electronic systems are difficult to realize experimentally, particularly for magnetically ordered systems. Here, we show that the van der Waals layered magnetic semiconductor CrSBr behaves like a quasi-1D material embedded in a magnetically ordered environment. The strong 1D electronic character originates from the Cr−S chains and the combination of weak interlayer hybridization and anisotropy in effective mass and dielectric screening, with an effective electron mass ratio of $m_X^e/m_Y^e \sim 50$. This extreme anisotropy experimentally manifests in strong electron−phonon and exciton−phonon interactions, a Peierls-like structural instability, and a Fano resonance from a van Hove singularity of similar strength to that of metallic carbon nanotubes. Moreover, because of the reduced dimensionality and interlayer coupling, CrSBr hosts spectrally narrow (1 meV) excitons of high binding energy and oscillator strength that inherit the 1D character. Overall, CrSBr is best understood as a stack of weakly hybridized monolayers and appears to be an experimentally attractive candidate for the study of exotic exciton and 1D-correlated many-body physics in the presence of magnetic order.**

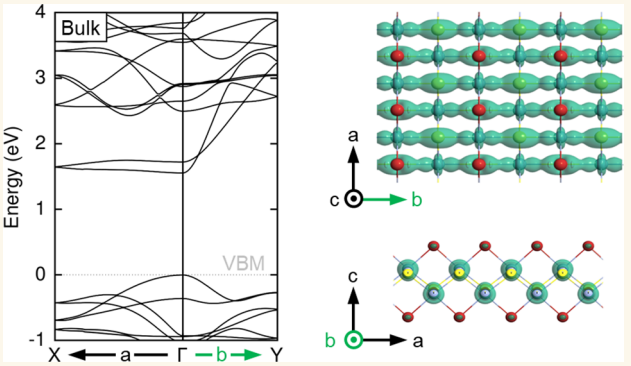

KEYWORDS: *CrSBr, van der Waals magnetic semiconductor, quasi-1D material, electron−phonon coupling, exciton−phonon coupling, anisotropic dielectric screening, van Hove singularity*

Experimental realizations of one-dimensional (1D) platforms for the study of quantum phenomena are rare; some examples include ultracold quantum gases,[1] atomic chains,[2] or carbon nanotubes.[3−8] While such platforms are essential for the study of correlated phenomena like Tomonaga−Luttinger liquids,[2,5] 1D spin chains,[9] or for the realization of quantum conducting wires,[10] they may be unstable, hard to scale up, or suffer from ensemble inhomogeneities. The recent emergence of the field of quasi-1D materials represents a technologically appealing alternative.[11] Quasi-1D materials are ideal systems to realize, study, and exploit strongly correlated phenomena in a solid-state platform. They are typically characterized by an anisotropy of the structural atomic arrangement and the related electronic intraplanar interactions in different crystallographic directions. Examples include MoS_2 nanotubes[12] and hBN nanotubes;[13] III−V-based nanowires;[14,15] or materials such as $ZrTe_3$,[16] $NbSe_3$,[17] or $TiSe_3$.[18] Low-dimensional systems with both electronic and magnetic character are particularly intriguing, and several efforts have been dedicated to their design and fabrication.[19] Early examples include dilute magnetic semiconductors, like Mn-doped quantum wells and quantum wires,

Received: July 22, 2022
Accepted: March 3, 2023
Published: March 16, 2023

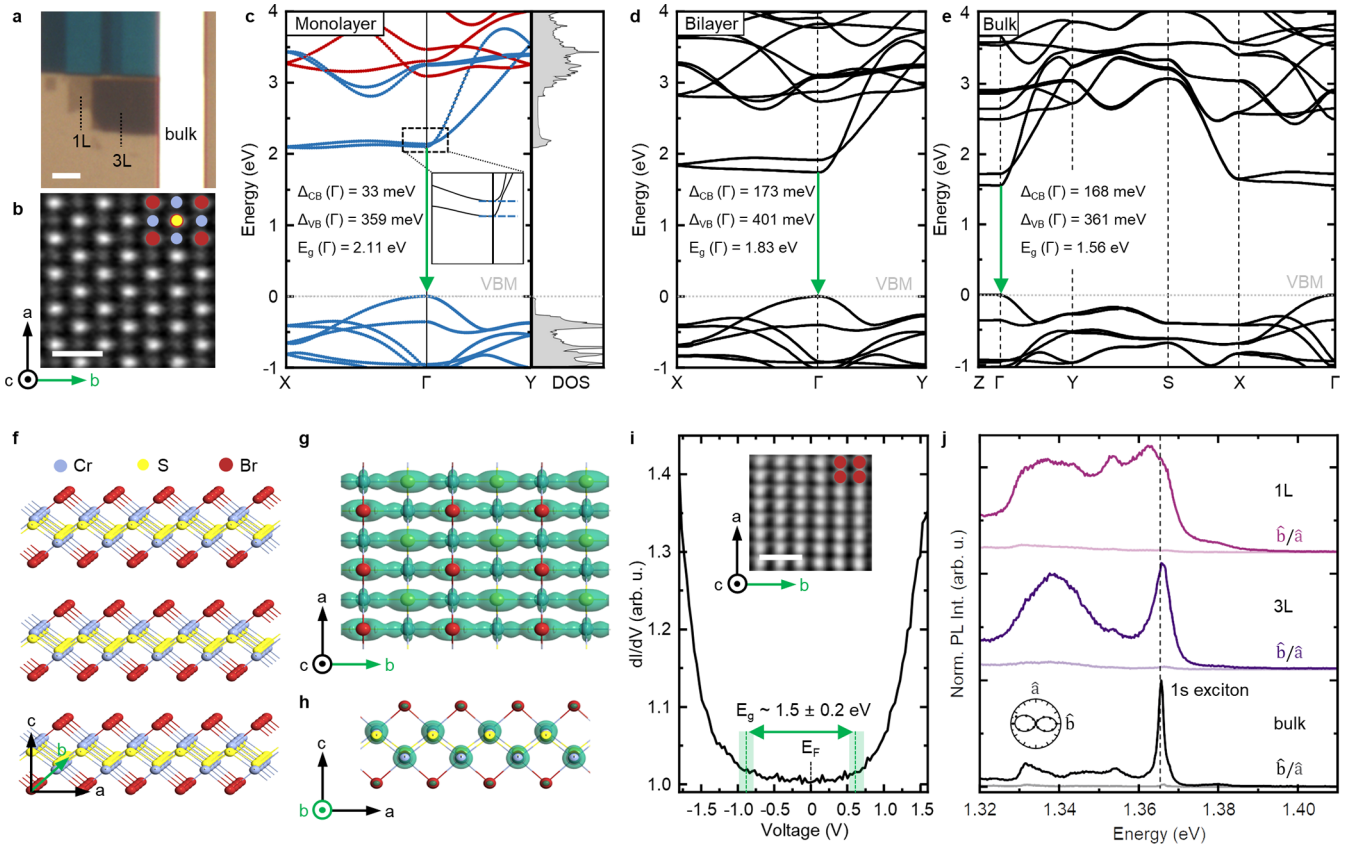

Figure 1. Quasi-1D electronic structure of CrSBr in the bulk. (a) Optical micrograph of mechanically exfoliated CrSBr. Needlelike crystals extend along the *a* direction. Scale bar is 4 μm. (b) STEM-HAADF image of multilayer CrSBr taken at an electron beam energy of 200 keV. Scale bar is 0.5 nm. (c) 1L CrSBr *GW* calculation of the high symmetry points *X*−Γ−*Y*, which shows a flat conduction band along the Γ−*X* direction (effective electron mass $m_X^e = 7.31m_0$) corresponding to the *a* direction, and a highly dispersive band along the Γ−*Y* direction ($m_Y^e = 0.14m_0$) corresponding to the *b* direction. The blue and red colors represent the majority and minority (in-plane) spin polarization. The corresponding density of states (DOS) is shown. Inset: magnification of the split conduction bands at Γ (Δ_{CB} = 33 meV). (d,e) *GW* calculations of 2L and bulk CrSBr. (f−h) Schematic illustration of bulk CrSBr by the relevant electronic structure formed mainly by Cr and S atomic orbitals. The charge density of states shown near the Fermi level is obtained by DFT calculations. The charge density includes the states in the range of 0.1 eV below the top of the valence band and 0.1 eV above the bottom of the conduction band. Although the atomic distance in the *a* direction is less than in the *b* direction, the electronic states form chains (charge density in green) along the *b* direction that are only weakly hybridized (coupled) along the *a* direction. (i) Room temperature constant height d*I*/d*V* from scanning tunneling spectroscopy (STS) (I_t = 50 pA at V_{bias} = 0.2 V) with a single-particle gap of ~1.5 ± 0.2 eV. Green error bars show the uncertainty from the CBM and VBM onset. Inset: Topographic STM image of CrSBr showing the Br atoms on the surface. Scale bar is 1 nm. (j) Low-temperature (4.2 K) PL of 1L, 3L, and bulk (36.8 nm, ~46L) CrSBr for the electric field copolarized in excitation and detection along the *b* and *a* direction, respectively. Excitation power is 100 μW. The PL emission of the 1s exciton in bulk CrSBr is highlighted. Inset: anisotropic 1s exciton emission of bulk CrSBr.

that exhibit electronic and optical excitations that are strongly correlated with the magnetic degree of freedom.[20,21]

Quasi-1D electronic systems that are also magnetic are expected to offer an even greater range of exotic quantum phenomena and functionalities. The recent observation of long-range magnetic order in van der Waals magnets[22,23] provides a prospect for the experimental realization of materials with correlated excitations, including electron−electron, electron-spin, exchange, and electron−phonon interactions. In one such magnet, TiOCl, spin-Peierls and charge density wave (CDW) physics have been reported.[24−26] TiOCl is a member of the group of chalcogen halides that are described by the stoichiometric formula MXP composed of a transition metal (M = Cr, Fe, V), a chalcogen (X = S, Se, O), and a halogen (P = Br, Cl, I). Without including spin, the chalcogen halides have space group 59 (*Pmmn*) and point group D_{2h}. The observation of correlated physics in TiOCl suggests that electronic 1D character may be visible in materials that have similar structure but even larger structural anisotropy.

One such material is CrSBr.[27−39] This is a semiconductor with a band gap of ~1.5 eV.[29,31] It is also an A-type antiferromagnet (AFM) with the magnetic easy axis along the *b* direction and a high Néel temperature of T_N ~ 132 K.[28,31] Significantly, CrSBr is a relatively stable material in air.[39] Recent works have shown structural phase transformations,[35] correlated magneto-optical[33,36,39] and magneto-transport[31,37,38] properties, and the coupling of excitons and magnons.[40] Moreover, a recent transport study has reported an unusual anisotropy in the electron conductivity along the *a* and *b* directions of CrSBr with striking ratios of up to 10^5, attributed to quasi-1D transport.[38]

On the basis of its stability and the optical, electronic, and magnetic properties, we believe that CrSBr is an outstanding candidate for the practical engineering of atomic-scale magnetic excitations that offer opportunities for nanospin-

https://doi.org/10.1021/acsnano.2c07316
ACS Nano 2023, 17, 5316−5328

tronic, nanospin-photonic, and memory devices. However, it is essential to first understand the origin of the peculiar electronic structure of CrSBr and its impact on the material's vibrational, optical, and magnetic properties and related quasiparticle interactions. In this manuscript, we have therefore examined the band structure, atomic structure, quasiparticles, and their mutual couplings in CrSBr both experimentally and theoretically. Our key finding is that CrSBr is unambiguously a quasi-1d material even in bulk exfoliated form. We explain this result by suggesting that CrSBr exhibits a strong 1D electronic character that is due to electronic chains that are weakly coupled within each layer in combination with a weak interlayer hybridization and anisotropy in effective mass and dielectric screening. This is further corroborated by our observation of a structural distortion along the direction of high electronic density, which is suggestive of a Peierls instability. Moreover, we find that all quasiparticle excitations and their mutual couplings that we measure experimentally using resonant and nonresonant Raman, low-temperature photoluminescence, magneto-reflectivity, and photoluminescence excitation spectroscopy can be understood through a dominant role of this low-dimensional electronic structure. Strikingly, optical spectroscopy on exfoliated bulk CrSBr shows ultraclean excitonic signatures with Lorentzian line widths of only 1 meV, a value usually known only from high-quality boron nitride-encapsulated monolayer semiconductors, like MoS_2 or WSe_2; we also attribute this to the 1D electronic character, in combination with the absence of sample inhomogeneity from strain or substrate/surface effects that dominate measurements from other materials that can only be measured as atomically thin layers. From our results, we propose that bulk CrSBr is best understood as a stack of weakly coupled monolayers that host quasi-1D excitons of high binding energy with strong quasiparticle interactions because of the quasi-1D electronic character in each layer. Our work establishes bulk CrSBr as an ideal platform to explore rich quasiparticle excitations and their mutual couplings in a magnetically ordered environment.

RESULTS AND DISCUSSION

Quasi-1D Electronic Structure of CrSBr. Unlike the previously investigated archetypal magnets CrI_3 and $Cr_2Ge_2Te_6$,[22,23] CrSBr shows good air stability and can be easily cleaved down to a monolayer (1L) (see Figure 1a).[39] Exfoliated crystals have a needlelike shape and exhibit structural anisotropy, which is apparent from the atomic arrangement in scanning transmission electron microscopy high-angle annular dark-field (STEM-HAADF) images (see Figure 1b).[35] The strong electronic anisotropy is directly apparent from our 1L, bilayer (2L), and bulk *GW* calculations (see Figure 1c–e). The 1L calculation shows two conduction bands (energy splitting of 33 meV at the Γ point) that are flat along the *a* direction but highly dispersive along the *b* direction. Here the *a* and *b* directions are defined as Γ−*X* and Γ−*Y*, respectively. The relevant electronic structure around the Γ point can also be well described in a simple three-band $k \times p$ model [see the Supporting Informtion (SI)]. The Γ point effective masses of the lowest conduction band and the highest valence band in the Γ−*X* and Γ−*Y* directions, respectively, are extracted from the *GW* band structures: $m_X^e = 7.31m_0$, $m_Y^e = 0.14m_0$, $m_X^h = 2.84m_0$, $m_Y^h = 0.45m_0$. This manifests as a pronounced effective electron mass anisotropy of $m_X^e/m_Y^e \sim 50$. This mass anisotropy is significantly higher than the value for anisotropic black phosphorus.[41] The electronic anisotropy originates from the orbital composition of the electronic bands around the conduction band minimum (CBM) and the valence band maximum (VBM). This is best visualized by the charge density around the Fermi level of CrSBr, with predominant admixture from the Cr−S chains along the *b* direction (see Figure 1g,h). The orbitals of the Br atoms only weakly admix into the conduction bands, thereby resulting in the weakened interlayer hybridization. In the case of the 1L, we obtain admixtures for the lower conduction band of 64% Cr, 32% S, and 4% Br and for the upper conduction band of 86% Cr, 9% S, and 5% Br for the upper conduction band. It is the dominant admixture of the Cr and S orbitals in the band structure that cause CrSBr's strong 1D electronic character, with a shallow 1D quantum confinement along the *a* direction due to a weak intralayer hybridization (coupling) of the chains. This weak hybridization is also apparent from the *GW* calculation of 2L and bulk CrSBr (see Figure 1d,e) and differs from semiconducting transition metal dichalcogenides (TMDCs).[42,43] We obtain a qualitatively similar band structure for 1L, 2L, and bulk along the *X*−Γ−*Y* direction, as expected from the weak interlayer hybridization. The fundamental band gap is direct and situated at the Γ point, in addition to a nearly degenerate conduction band state at the *X* point for the 1L. In general, we find that the effect of the flat band along Γ−*X* becomes even more pronounced in the *GW* calculation. Moreover, the strong mass anisotropy results in a large density of states (DOS) along the Γ−*X* direction at the band edge, which is expected to be accompanied by a van Hove singularity (see the SI). However, it should be noted that this is only slightly apparent from the calculated DOS (see Figure 1c) because of the admixture of bands from all momenta that makes this effect less pronounced.

In order to access the electronic states experimentally, we perform scanning tunneling microscopy (STM) and spectroscopy (STS) at room temperature (T = 300 K) on bulk CrSBr crystals cleaved under ultrahigh vacuum to obtain a clean surface. Figure 1i shows a typical dI/dV trace. The extracted size of the band gap, $E_g = 1.5 \pm 0.2$ eV, is consistent with the bulk *GW* calculation yielding an energy gap of 1.56 eV (see Figure 1e) and in agreement with a previous STS study.[31] However, the position of the Fermi level E_F in our material suggests a more intrinsic behavior, likely from a lower density of defects.[31]

Low-temperature (4.2 K) PL (see Figure 1j) confirms the weak interlayer hybridization of CrSBr, which is in line with the other findings. The optical emission of CrSBr is strongly linearly polarized along the *b* direction, thereby reflecting the electronic anisotropy. The spectra from 1L, 3L, and bulk (36.8 nm, ∼46L) show a clear signature of the 1s exciton recombination at ∼1.366 eV along with other hitherto unidentified peaks below the 1s exciton in energy. Most importantly, the features in all spectra remain the same upon layer number reduction, but display significant line broadening that likely originates from disorder-related effects such as strain, unintentional doping from the substrate, defects, or adsorbates. For bulk CrSBr, we obtain Lorentzian line widths of the 1s exciton of ∼1 meV, which is reminiscent of high-quality hBN-encapsulated TMDCs.[44,45]

Anisotropic Structural Distortion. Next, we collect STEM-HAADF images of exfoliated CrSBr flakes from the bulk thickness down to the monolayer (see 2L and 4L in Figure 2 and additional layer numbers in the SI) in order to

https://doi.org/10.1021/acsnano.2c07316
ACS Nano 2023, 17, 5316−5328

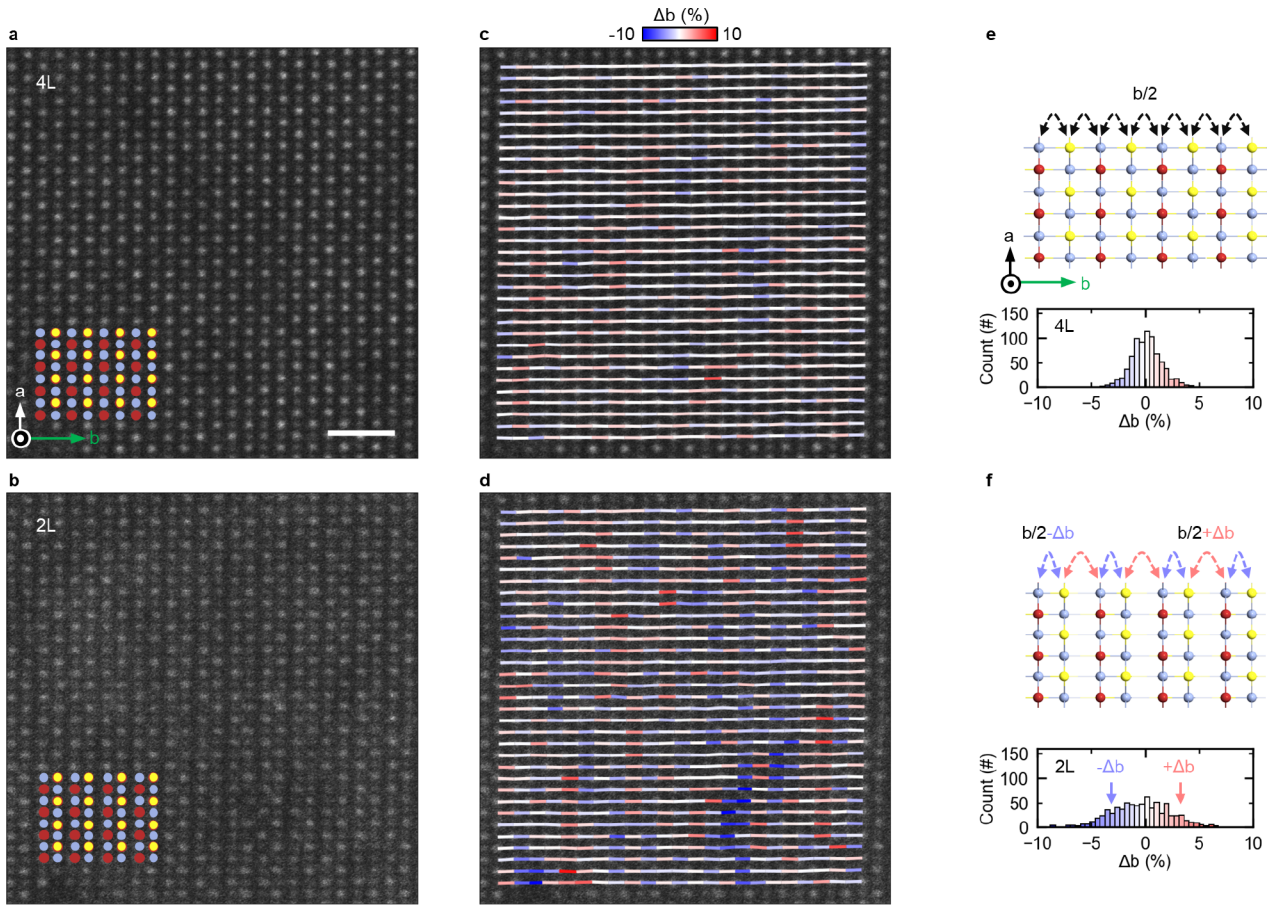

Figure 2. Anisotropic structural distortion along the *b* direction in CrSBr. (a,b) STEM-HAADF image of a 4L and 2L CrSBr flake. Image was taken at room temperature (300 K), a beam energy of 200 keV, and a beam current of 40 pA. The inset shows the atomic arrangement. Scale bar is 1 nm. (c,d) Corresponding visualization of the percentage change of interatomic distance Δb between the Cr and S/Br atomic columns along the *b* direction. The distances are normalized to the pristine nondistorted distance $b/2$ of a 6L CrSBr. (e) Schematic illustration of the nondistorted atomic arrangement without a structural distortion, as further corroborated from the histogram of 4L CrSBr obtained from (c). (f) Schematic illustration of the atomic distortion along the *b* direction. The absolute lattice distances along the *b* direction are characterized by $b/2 \pm \Delta b$. The corresponding histogram of a 2L CrSBr from the analysis in (d) shows additional characteristic shoulders at $\pm\Delta b \sim \pm 4\%$ from the alternating line pairs.

probe structural changes that arise from the anisotropic electronic structure of CrSBr. Strikingly, we observe a structural dimerization of the crystal lattice along the *b* direction forming line pairs as the layer number is reduced (see Figure 2c). This is not just a simple surface effect since we do not observe this structural distortion in STM topographic images (see inset Figure 1i).[36] Importantly, this coincides with the direction of the strong quasi-1D electronic structure of CrSBr (see Figure 1g). We further visualize and quantify this structural distortion by analyzing the percentage change in the interatomic lattice distance Δb (see Methods) between neighboring Cr and S/Br atomic columns along the *b* direction (see Figure 2c,d). The corresponding extracted percentage change in the interatomic distances along the *b* direction is shown in histograms in Figure 2e,f. We observe a significant structural distortion that becomes increasingly more dominant when the layer number of CrSBr is reduced. The bilayer exhibits a broadened distribution with characteristic shoulders at $\pm\Delta b$ that reflect the expansion and contraction of the chains. We obtain large structural distortions of $\Delta b \sim \pm 4\%$ that are comparable with highly correlated materials like 1T-TaS_2.[46] All histograms remain centered around 0% for all layer numbers, thereby suggesting no buildup of net strain. Notably, for the 1L, we observe almost fully isolated line pairs that form 1D-like nanowire structures (see SI). Moreover, there is no structural distortion along the *a* direction (see SI).

The formation of line pairs along the *b* direction is a hallmark signature of a quasi-1D material suggestive of a Peierls distortion.[11] This observation further supports the strong electronic anisotropy of CrSBr visible from a change in the atomic arrangement. The magnitude of the structural distortion is directly related to the strength of the electron−phonon coupling of the system.[47] The high value (±4%) observed for CrSBr is suggestive of very large electron−phonon coupling effects. We note that the exact amount of lattice distortion is likely to further depend on pressure and temperature. The intricate interdependence of layer thickness, strain, and electronic structure further provides fertile grounds for future studies.

Quasi-1D Electron−Phonon Coupling. The pronounced quasi-1D electronic structure and band anisotropy is expected to manifest itself in the quasiparticle excitations and their mutual interactions. From the observed structural distortion suggestive of a Peierls instability, we already expect a strong electron−phonon coupling in CrSBr. To explore such interactions between excitations of the 2D lattice and

https://doi.org/10.1021/acsnano.2c07316
ACS Nano 2023, 17, 5316−5328

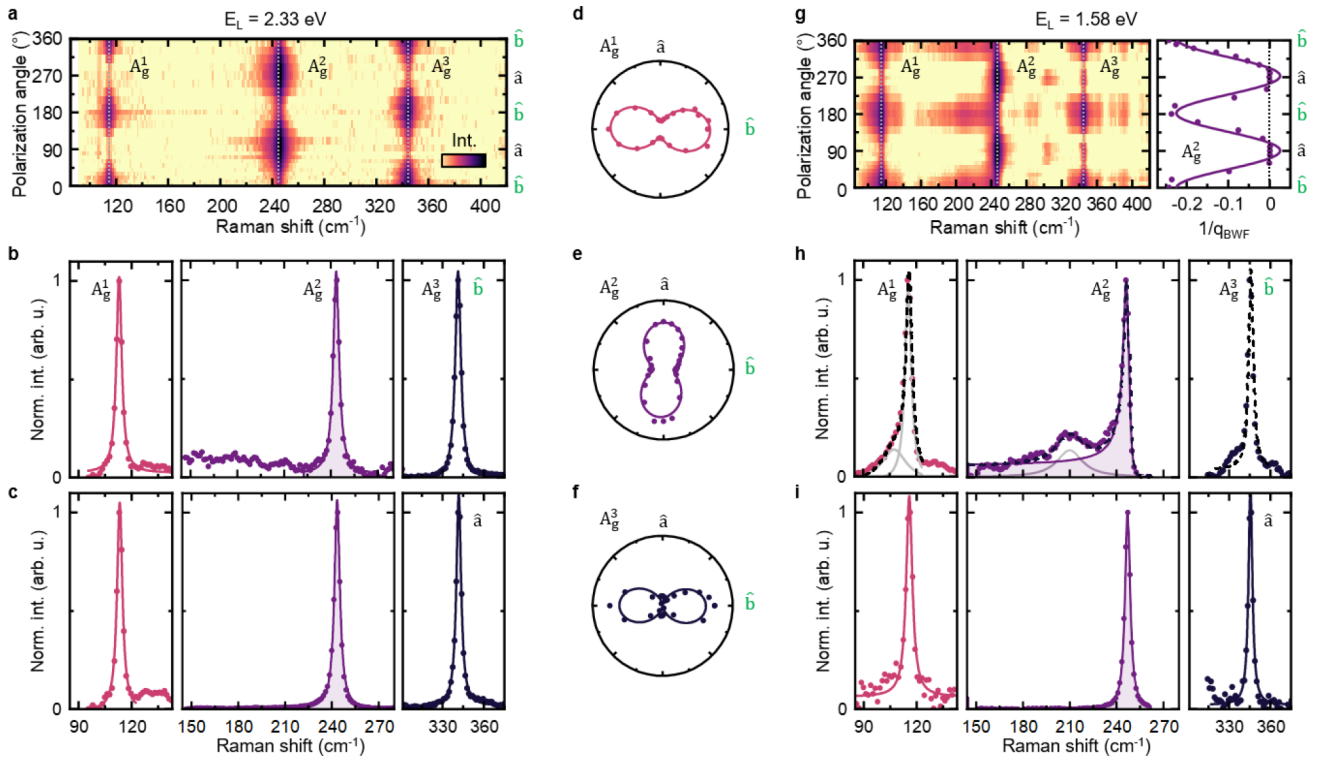

Figure 3. Pronounced and quasi-1D electron−phonon coupling in bulk CrSBr. (a) False color mapping of the polarization angle-dependent Raman spectra with off-resonant excitation at E_L = 2.33 eV far above the single-particle gap, for an excitation power of 250 μW at room temperature. The three main phonon modes A_g^1 (115 cm^{-1}), A_g^2 (245.5 cm^{-1}), and A_g^3 (344 cm^{-1}) in CrSBr are highlighted. (b) Normalized Raman spectra for each individual mode with polarization along the *b* direction ($\hat{b}$, 0° or 180°) shows Lorentzian line shapes, as does (c) the *a* direction ($\hat{a}$, 90° or 270°). (d−f) Polarization angle-dependent intensity of the A_g^1, A_g^2, and A_g^3 phonon mode for excitation at E_L = 1.58 eV and an excitation power of 1000 μW. Only mode A_g^2 exhibits an intensity maximum along the $a\hat{a}$ direction. The solid lines are sin^2 fits. (g) Left: polarization-dependent Raman at an excitation energy of E_L = 1.58 eV that is in electronic resonance with the band gap. Right: the Breit−Wigner−Fano coupling parameter $1/q_{BWF}$ of the A_g^2 phonon mode oscillates between the *b* and *a* directions, as further indicated by the sine fit. (h) Normalized Raman spectra for each individual mode with the electric field copolarized along the *b* direction. The A_g^2 mode is fitted with a BWF resonance (see eq 1). (i) Raman spectrum along the *a* direction. All modes exhibit fully Lorentzian line shapes.

excitations of the quasi-1D electronic system, we perform resonant inelastic light scattering (RILS) spectroscopy.[48] In order to probe the quasiparticles of the lattice excitations selectively, we use nonresonant Raman with an excitation well above the band gap of E_L = 2.33 eV; to study the interaction between the quasiparticles' electronic interband, intraband, and lattice excitations, e.g., electron−phonon and exciton−phonon, we perform resonant Raman with excitation close to the single-particle band edge of CrSBr (E_L = 1.58 eV). For this measurement, we coalign linear excitation and detection polarizations and collect spectra of a bulk CrSBr flake (~20 nm) as a function of orientation with respect to the crystal axes.

The contour map for nonresonant excitation (E_L = 2.33 eV) shows three main modes that we identify as the A_g^1 (115 cm^{-1}), A_g^2 (245.5 cm^{-1}), and A_g^3 (344 cm^{-1}) modes (see Figure 3a) analogously to the modes observed in CrOCl.[49] While all modes are due to out-of-plane atomic displacements, the A_g^1 and A_g^3 modes exhibit an intensity maximum along the $\hat{b}$ direction while the A_g^2 mode exhibits a maximum along the *a* direction (see Figure 3d−f). Importantly, the line shape of all modes is Lorentzian for all polarization angles.

For resonant excitation (E_L = 1.58 eV), we observe a number of additional resonant modes with distinct energies and a very pronounced asymmetric line shape of the A_g^2 mode (see Figure 3g−i), but only when the electric field vector is aligned along the *b* direction (*k*-vector pointing along the *a* direction). This asymmetry is absent for the same experimental conditions in CrOCl, which rules out a laser-induced origin (see SI). This line shape can be interpreted as a signature of pronounced electron−phonon interactions in the presence of resonance effects, e.g., coupling between lattice and electronic excitations.[3,4] A potential interpretation is a strong polarization-selective 1D-like electron−phonon interaction of the A_g^2 mode with the electronic structure. The A_g^2 mode is polarized along the *a* direction and is, therefore, prone to strongly couple to the high DOS of the electronic system along the Γ−X direction (see Figure 1c). This is known as a Breit−Wigner−Fano (BWF) resonance, with the phonon as the discrete state and the 1D DOS along the *a* direction as the electronic continuum from shallow 1D quantum confinement.[3,4] The spectral form of a BWF resonance is given by

$$I(\omega) = I_0 \frac{[1 + (\omega - \omega_{BWF})/(q_{BWF}\Gamma)]^2}{1 + [(\omega - \omega_{BWF})/\Gamma]^2} \quad (1)$$

where the asymmetry factor $1/q_{BWF}$ characterizes the coupling strength between the phonon and the electronic continuum, and ω_{BWF} is the uncoupled BWF peak frequency. The BWF resonance profile reproduces the experimental A_g^2 mode spectrum under resonant excitation along the *b* direction (see Figure 3b). The BWF coupling parameters $1/q_{BWF}$ deduced from those fits (see right panel, Figure 3g) reveal a

https://doi.org/10.1021/acsnano.2c07316
ACS Nano 2023, 17, 5316−5328

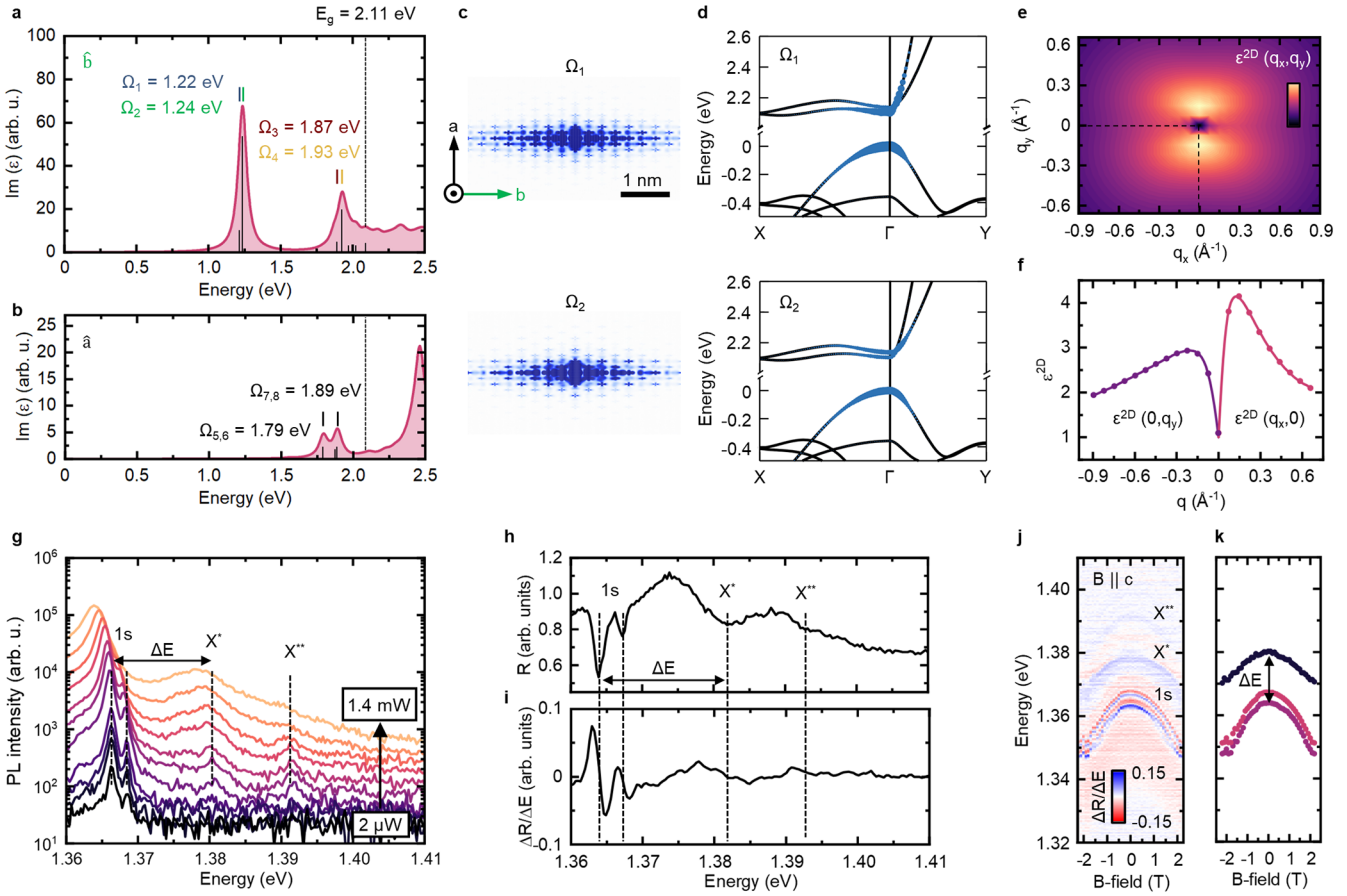

Figure 4. Quasi-1D excitons with high binding energy from dielectric and mass anisotropy in CrSBr. (a) Calculated optical absorption spectrum obtained ab initio by solving the BSE of 1L CrSBr with an electric field polarized along the *b* direction (Γ−*Y* direction). The spectrum shows four excitonic resonances. Ω_1 and Ω_2 originate from the two split conduction bands with a small energy splitting of $\Delta E_{\Omega_1,\Omega_2} \sim 20$ meV. The binding energies are given by 0.88 and 0.90 eV for Ω_1 and Ω_2, respectively. Ω_3 and Ω_4 are excitons from energetically higher lying bands. (b) Calculated optical absorption spectrum from ab initio BSE of 1L CrSBr for the electric field polarized along the *a* direction (Γ−*X* direction) showing the strong electronic anisotropy and the absence of Ω_1 and Ω_2. (c) Corresponding anisotropic real-space exciton wave function of Ω_1 and Ω_2. (d) Momentum-space exciton compositions of Ω_1 and Ω_2 have large band contribution along the Γ−*X* direction. (e) Calculated macroscopic momentum-dependent dielectric function $\epsilon^{2d}(q_x, q_y)$ of freestanding 1L CrSBr exhibiting a strong anisotropy along q_x and q_y. (f) $\epsilon^{2d}(0, q_y)$ and $\epsilon^{2d}(q_x, 0)$ as a function of q. First-principles results are shown by dots, while solid lines are a guide to the eye. (g) Low-temperature (4.2 K) PL as a function of excitation power of bulk CrSBr. The spectrum shows a double resonance for the 1s exciton (~1.366 eV) due to the finite thickness of the flake (~36.8 nm), and two signatures *X and *X*** at 1.380 and 1.391 eV, respectively. The energy splitting between the 1s exciton and *X** is Δ*E* ~ 15 meV. (h) Reflectance contrast *R* taken at 1.6 K showing the same resonances. (i) Corresponding derivative Δ*R*/Δ*E*. (j) False color plot of the magnetic-field-dependent differential reflectivity Δ*R*/Δ*E* with the *B* field applied parallel to the *c* axis. The data show the 1s exciton, *X**, and a faint signature of the *X***. (k) Position of the 1s exciton doublet and *X**.**

high coupling strength between phonons and an electronic continuum of $1/q_{BWF} = -0.24$ for polarization along the *b* direction. This is comparable with values for metallic CNTs reported between −0.2 and −0.6.[6−8] In contrast, the line shape of the RILS spectra of A_g^2 measured along the *a* direction is best described by a pure Lorentzian with $1/q_{BWF}$ yielding a vanishing coupling between phonons and the electronic continuum. The observation of the highly anisotropic Fano resonance can serve as a strong signature for the 1D nature of the continuum.[6−8] While the observation of a Fano line shape is surprising in a semiconductor like CrSBr, this is not limited to metallic systems like CNTs but this phenomenon is also observed in gapped materials that generally exhibit pronounced electron−phonon interactions.[50,51] CrSBr has shown a high intrinsic carrier concentration of ~10^{13} cm^{-2}[37] in agreement with a high concentration of Br vacancy defects[36] that induce n-doping in the material, which shifts the Fermi level close to the conduction band. Moreover, low-dimensional behavior and Fano physics[52] have also been observed in TiOCl, thereby suggesting that this is likely a universal effect in materials that are of FeOCl-type. However, other possible interpretations exist. For example, the line shape can be affected by resonance modes from different points in momentum space. Additional insight into the Raman process is required to further elucidate the physics of the line shape of the A_g^2 mode and the complex resonance Raman spectrum of CrSBr.

The observed 1D nature of the electronic system in this 2D van der Waals material with 3D spin-exchange interaction is unexpected. We can understand the behavior by considering the flat conduction band along the Γ−*X* direction with its very large DOS (see Figure 1c). Under the assumption that the

https://doi.org/10.1021/acsnano.2c07316
ACS Nano 2023, 17, 5316−5328

lattice excitations (phonons) couple to the highly anisotropic electronic continuum (collective excitations of electrons), we expect the BWF coupling term (between the electronic continuum and the discrete phonon line) to be proportional to the DOS at E_F. In the resonant Raman process, the excited phonons from the interband excitation can couple via intraband scattering processes to the continuum of electronic states in the lowest CB that are confined into a quasi-1D system. Using the 1D model for carrier dynamics (see SI), we can estimate this DOS to be $\nu(E) = \sqrt{2m^*/E}\,(1/2\pi l)$, where m^* is the effective mass in the dispersive direction, l is the effective interchain distance, and E is the energy relative to the conduction band minimum. For carrier density n_{el}, we find that this DOS scales as $\nu(E_F) \sim m^*/(\pi^2 l^2 n_{el})$, which yields a large number of electron−hole excitations that can hybridize with the phonon mode.

Quasi-1D Excitons with Large Binding Energy. CrSBr exhibits a rich optical spectrum with several peaks that are not yet identified.[33,36,40] The quasi-1D electronic structure of CrSBr is expected to directly affect the properties of the Coulomb-bound quasiparticle excitations. To evaluate the implications of the quasi-1D electronic structure on the complex optical spectrum, we calculate excitonic properties of monolayer CrSBr on the basis of *GW* and Bethe−Salpeter equations (BSE) and compare them with experimental signatures from optical PL and reflectivity measurements. Results for the calculated excitonic spectrum are shown for the electric field polarized along the *b* and the *a* directions (see Figure 4a,b). We identify four excitonic resonances in the *b* direction: $\Omega_1 = 1.22$ eV, $\Omega_2 = 1.24$ eV, $\Omega_3 = 1.87$ eV, and $\Omega_4 = 1.93$ eV. The two energetically lowest excitons are split by only $\Delta E = 20$ meV. This energy difference has its origin in the two energy-split conduction bands (see inset Figure 1c). We obtain large binding energies for $E_b(\Omega_1) = 0.88$ eV and $E_b(\Omega_2) = 0.90$ eV. The corresponding real-space representation of the excitonic wave functions of Ω_1 and Ω_2 suggest a strong 1D character with the excitons extended along the *b* direction but squeezed along the *a* direction (see Figure 4c). The origin is the predominant orbital admixture from the flat conduction bands along the Γ−*X* direction (see Figure 4d). For the most important orbitals, we obtain an admixture for the lower conduction band of 61% $d_{(x^2-y^2)}$, 10% $d_{(3z^2-r^2)}$, and 27% p_z and for the upper conduction band of 61% $d_{(x^2-y^2)}$, 25% $d_{(3z^2-r^2)}$, and 7% p_z. Importantly, the anisotropy is found not only in the effective electron mass along Γ−*X* and Γ−*Y* but also dominating the dielectric function $\epsilon^{2D}(q_x, q_y)$ in reciprocal space (see Figure 4e,f) and is shown in the real and imaginary part of the macroscopic dielectric function in both the monolayer and the bulk (see SI). It is this intricate interplay of effective mass anisotropy and dielectric anisotropy that shows in the quasi-1D character of the excitonic quasiparticles in CrSBr.

We now probe the excitonic signatures of bulk CrSBr at low temperature (4.2 K) by nonresonantly exciting the system with a continuous-wave laser at an energy of 2.384 eV (see Figure 4g). We observe that the 1s exciton at an energy of ∼1.366 eV (at an excitation power of 10 μW) appears as a doublet, likely because of a cavity effect (interference effects) caused by the thickness of the crystal (∼36.8 nm) (see SI).[53] We obtain a very sharp Lorentzian peak with a full width at half-maximum (fwhm) of ∼1 meV, thereby verifying high homogeneity of the parallel, weakly coupled chains in combination with the high crystal quality. The 1s exciton red-shifts with increasing excitation power, as is typically observed for increasing numbers of photogenerated carriers in other semiconducting van der Waals materials (also see SI).[54] Moreover, for high excitation powers, additional resonances above the 1s exciton, labeled *X** and *X***, appear at energies of 1.380 and 1.391 eV, respectively. While they are weakly visible in PL, their appearance in the low-temperature (1.6 K) reflectance contrast measurements and derivative (see Figure 4h,i) suggests finite oscillator strength and band-related transitions. The energy splitting of the 1s exciton and the *X** is only $\Delta E \sim 15$ meV.

We next measure the impact and potential origin of the magnetic order and exchange interaction between the magnetic moments in the 3D matrix and the quasi-1D excitons by probing the 1s exciton, *X**, and *X***, at 1.6 K in reflectivity, as a function of a magnetic field along the *c* axis (see Figure 4j). The signatures show the expected magnetic field-dependent energy shift due to the change in magnetic ordering from AFM to FM until reaching the coercive field of 2 T (see Figure 4j,k). The energy shift of the *X** is weaker than the 1s exciton. The *X*** is weak in signal for higher fields but the data suggests an energy shift qualitatively similar compared to that of the *X** (see Figure 4j).

The attribution of the *X** and *X*** is nontrivial. Potential scenarios would involve momentum direct or indirect transitions between the split conduction bands and the valence band. It is, indeed, a possibility that these transitions are more complex in nature with a momentum indirect character because of the strong extension of the wave function along the Γ−*X* direction. Such a transition can furthermore be phonon-assisted.

The energetic shift in the magneto-reflectivity data of the 1s exciton and the *X** and *X*** suggests that the main orbital composition is likely still from the two split conduction bands. At the Γ point in bulk CrSBr, the orbital composition of the lower conduction band is 59% $d_{(x^2-y^2)}$, 21% $d_{(3z^2-r^2)}$, and 10% p_z, while for the upper conduction band, it is 60% $d_{(x^2-y^2)}$, 5% $d_{(3z^2-r^2)}$, and 34% p_z. The upper conduction band has a much lower admixture of Cr $d_{(3z^2-r^2)}$ orbitals, which suggests a scenario in which the exciton reacts less to an external magnetic field since the magnetic moment is situated on the d orbital. This might indicate a potential origin of the *X** and *X*** from a transition that involves the upper conduction band. In general, the excitonic transitions are expected to inherit the orbital character, and this should also be the case for potential indirect transitions that preserve the orbital conduction band admixture away from the Γ point. This further illustrates that the quasi-1D electronic structure and related orbital admixture have direct consequences on the magneto-optical coupling of the excitonic complexes in CrSBr.

Pronounced Exciton−Phonon Coupling and Rich Electronic Structure. In the last part of this investigation, we further confirm our interpretation of CrSBr as a quasi-1D material in the bulk limit by studying the electronic structure and quasiparticle interactions of CrSBr using high-resolution photoluminescence excitation spectroscopy (PLE) measurements. We spectroscopically probe CrSBr at low temperature ($T = 4.2$ K) by tuning a continuous-wave laser in small steps over a wide energy range from 1.39 to 1.76 eV and collect the PL from the 1s exciton, with excitation and detection copolarized along the *b* direction. Figure 5a shows a false

https://doi.org/10.1021/acsnano.2c07316
ACS Nano 2023, 17, 5316−5328

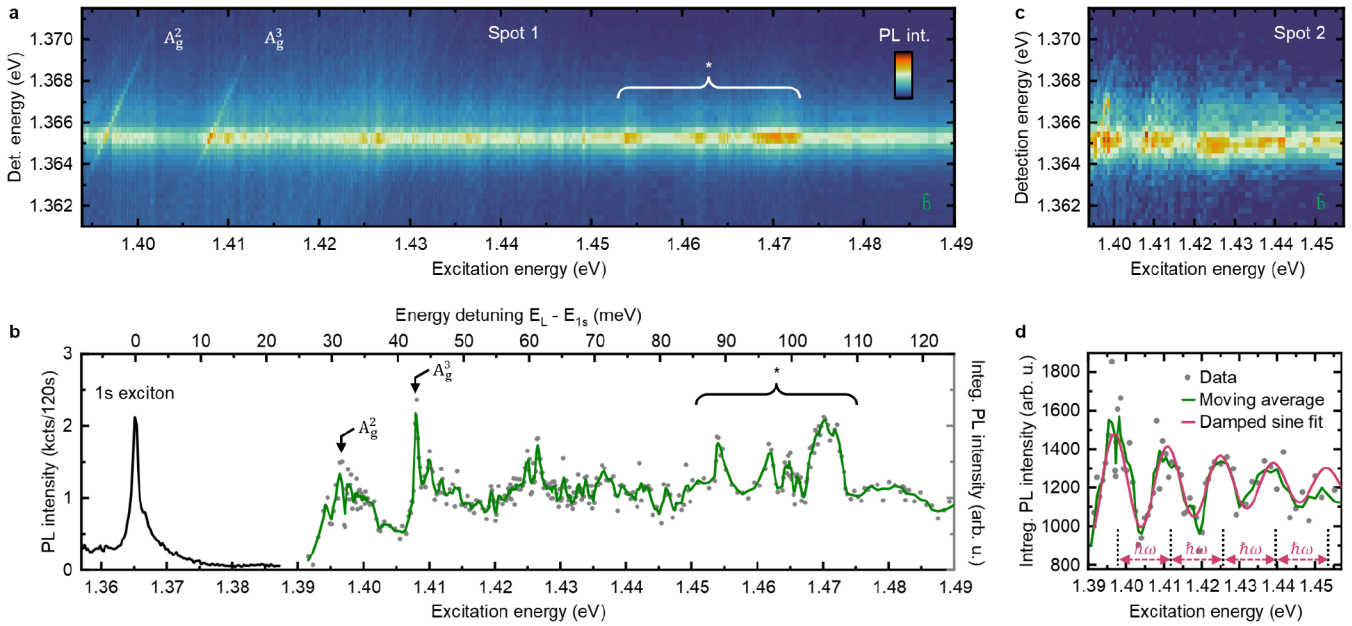

Figure 5. Pronounced exciton−phonon coupling and rich electronic structure in bulk CrSBr. (a) False color low-temperature (4.2 K) photoluminescence excitation spectroscopy (PLE) mapping of the 1s exciton at an emission energy of ∼1.365 eV. The 1s exciton shows resonant exciton−phonon coupling with two discrete phonons (A_g^2 and A_g^3) and additional electronic resonances highlighted with arrows. For the measurement, an excitation power of 100 μW is used. (b) PL emission spectrum of the 1s exciton at E_L = 1.406 eV. Integrated intensity of the 1s exciton is shown as a function of laser excitation energy. The green line is a moving average of three consecutive points to the data. The energies of the A_g^2 and A_g^3 are highlighted. At higher energies (E > 1.45 eV), additional distinct energy resonances (*) are observed and highlighted. (c) The PLE mapping at a second position with a lower energy resolution shows an oscillatory behavior in the intensity of the 1s exciton. (d) Corresponding integrated intensity of the 1s exciton as a function of laser excitation energy. The green line is a moving average of three consecutive points to the data. The purple line is an exponentially damped sin fit to the data with a characteristic energy of $\hbar\omega$ = 13.99 ± 0.25 meV (see dashed lines). For the measurement, an excitation power of 100 μW is used.

color contour plot of the 1s exciton PL as a function of the excitation energy, with the corresponding integrated 1s exciton intensity shown in Figure 5b. The PLE measurement exhibits an intricate fine structure with several features and resonances. Two energetic regions are of particular interest. In the energy range (E < 1.45 eV) close to the 1s exciton (∼1.365 eV), phonons play an important role. Here, we observe two distinct lines crossing the 1s exciton PL signal. We interpret these lines as resonant Raman signatures that suggest pronounced exciton−phonon coupling between two discrete phonons with the 1s exciton. Such signatures appear in the spectra when the energy detuning of the laser photon and the 1s exciton equals a phonon or multiple phonon energies, thereby leading to the resonant enhancement of the exciton emission. The two phonon lines cross with the 1s exciton at energy detunings of ∼31.1 meV (∼249 cm^{-1}) and ∼42.9 meV (∼343 cm^{-1}), respectively. The energies are in excellent agreement with the energies of the A_g^2 and A_g^3 phonon modes (see Figure 3). Pronounced exciton−phonon coupling effects are usually observed for 2D materials like hBN-encapsulated TMDCs[45,55] as a consequence of narrow exciton line widths, intrinsically high oscillator strength and high phonon DOS ∝ q[45] but are very pronounced even in our measurement, which further reflects the low-dimensional character of CrSBr in the bulk limit.

In the same energy range (E < 1.45 eV), we also observe oscillations in the 1s exciton emission intensity with equidistant energies with respect to the 1s exciton emission. These oscillations become even more apparent when collecting similar data on a second position, but with a lower energy resolution, to sample less fine structure (see Figure 5c,d). The intensity of the 1s exciton shows an oscillatory intensity modulation with a characteristic energy of 13.99 ± 0.25 meV (112 ± 2 cm^{-1}) as obtained from an exponentially damped sin fit (see dashed lines in Figure 5d). This energy is in excellent agreement with the A_g^1 phonon mode energy (14.3 meV) (see Figure 3). An optically dark phonon replica above the 1s exciton in energy has also been observed in $NiPS_3$[56,57] and interpreted as optically dark magnetic-bound exciton−phonon states. A reduced energy of this bound state is expected.[56,58] The observation of such signatures above the exciton in bulk CrSBr further illustrates the strong orbital and quasiparticle interactions that likely originate from the reduced dimensionality.

Finally, for higher energy detunings (E > 1.45 eV), we observe a sequence of additional resonances in the 1s exciton emission that are close in energy to the single-particle gap (see peaks labeled with * in Figure 5a,b). In this energy range, Rydberg states can be expected in bulk CrSBr. In general, the anisotropic, quasi-1D screening is expected to result in a divergence of the 1s state, thereby increasing the energy splitting between the 1s and 2s state. While our results provide initial insights into the complex electronic structure of CrSBr, additional measurements and theory are required to understand potential excited states in this material.

CONCLUSIONS

We have provided strong experimental and theoretical evidence that bulk CrSBr is a quasi-1D material. The quasiparticles in CrSBr and their mutual couplings illustrate a 1D electronic character that offers very clean experimental

https://doi.org/10.1021/acsnano.2c07316
ACS Nano 2023, 17, 5316−5328

signatures in addition to the magnetic order. We find that this material offers exciting opportunities to study the physics of quasi-1D electronic systems that are highly interacting, with vibrational, optical, and excitonic excitations and magnetic orderings of mixed dimensionalities.

The energetic flat band along the *a* direction ($\Gamma-X$ direction) motivates more detailed studies of potentially correlated behaviors in this material. This is further suggested by our observation of a structural distortion in thin layers of a Peierls instability. Generally, 1D systems are known to have strong tendencies toward charge-density-wave order via Peierls instability, which is also consistent with the observation of pronounced electron−phonon interaction in this system. It is also expected that at low densities other phases may compete and be favored. In particular, since the Coulomb interaction is long-ranged in the absence of free carriers, it is possible that at low carrier densities the system may instead tend toward a 1D Wigner crystal[59] or a stripe phase[60,61] given that the kinetic energy is already largely quenched in 1D while the Coulomb interaction remains long-range (see theoretical considerations in the SI).

CrSBr is a fascinating material that exhibits an intriguing electronic structure. We suggest that bulk CrSBr is best characterized as a stack of weakly coupled monolayers that each host excitons with large binding energies. The rich magnetic phase diagram contributes additional complexity, which renders it an ideal platform for exploring fundamental physics and exciting applications. We anticipate that the 1D electronic character will prove to be a universal feature of the chalcogen-halide materials, and signatures of this are likely to be expected in other related compounds.

METHODS

Crystal Growth and Sample Fabrication. CrSBr bulk crystals were grown by chemical vapor transport.[35] Samples were fabricated by mechanical exfoliation onto SiO_2/Si substrates. Sample thickness was verified by a combination of atomic force microscopy, optical phase contrast, and Raman spectroscopy. For the electron microscopy studies, exfoliated flakes were transferred to TEM-compatible sample grids using cellulose acetate butyrate (CAB) as the polymer handle. Subsequently, the CAB was dissolved in acetone, and the TEM grids were rinsed in isopropanol prior to critical point drying.

Raman Spectroscopy. Resonant and nonresonant Raman measurements were performed on a Renishaw inVia micro-Raman confocal microscope. For the measurements, we used a 100× objective with a laser spot size of ∼1 μm. The laser excitation power used for the measurements taken at 785 and 532 nm was 1000 μW and 250 μW, respectively. Ten individual spectra acquired at 20 s were averaged to result in a spectrum with a total integration time of 200 s. To adjust the polarization, we used a linear polarizer in the excitation and detection path that we copolarized. To change the polarization angle, the sample was placed on a rotating stage.

Photoluminescence Spectroscopy. For the PL measurements, we mounted the sample in closed-cycle helium cryostats (Montana Instruments or attoDRY 800) with a base temperature of 4.2 K. In both setups, measurements were made through the side window using a home-built confocal microscope with a 100×, 0.9 NA objective (Olympus). We excited the sample using a continuous-wave (CW) laser at 2.384 or 1.746 eV. The PL was collected confocally after using a long-pass filter. For the polarization-resolved PL, we used a linear polarizer in both excitation and detection and a half-wave plate to rotate the polarization. The light was fiber-coupled and directed to a high-resolution spectrometer that was attached to a liquid-nitrogen-cooled charge-coupled device camera.

Photoluminescence Excitation Spectroscopy. For the PLE measurements, we used a tunable CW Ti:sapphire laser (MSquared Solstis) that is highly monochromatic with a line width of 10^{-6} nm. The wavelength was locked using a wavemeter (High Finesse WS8). After wavelength tuning, we adjusted the excitation power to 100 μW before the microscope objective. Measurements were taken with the half-wave plate rotated such that the electric field pointed along the *b* direction. The light was fiber-coupled and subsequently dispersed using a high-resolution spectrometer attached to a liquid-nitrogen-cooled charge-coupled device camera.

Magneto-Optical Spectroscopy. For the magnetic field-dependent optical measurements, we mounted CrSBr bulk flakes on top of a SiO_2/Si substrate into a closed-cycle cryostat (attoDRY 2100). We cooled the sample to a lattice temperature of around 1.6 K. The magnetic field of a superconducting solenoid magnet was aligned along the *c* axis of the crystal with a maximum field up to 9 T. We fiber-coupled a broadband light source on the input to perform magnetic field-dependent reflectance measurements. The signal from the sample was collected using a second fiber and directed toward a high-resolution spectrometer attached to a liquid-nitrogen-cooled charge-coupled device camera. The broadband laser excitation power was set to 100 μW.

Scanning Tunneling Microscopy. The topographic images were taken at room temperature with a Unisoku UHV-LT four-probe scanning tunnelling microscope operated with a Nanonis controller and equipped with a scanning electron microscope that allowed the precise location of scan areas. The CrSBr bulk crystal was cleaved under vacuum to obtain a clean sample surface. Using PtIr tips, we acquired differential conductance (dI/dV) spectra using a lock-in amplifier. During data acquisition, the feedback loop was switched off.

Scanning Transmission Electron Microscopy. STEM imaging was performed with a probe-corrected Thermo Fisher Scientific Themis Z G3 operated at 200 kV. The probe convergence semiangle was 19 mrad. The corresponding probe size of the aberration-corrected electron beam was sub-angstrom. The typical beam current used was 40−60 pA. All images were collected at room temperature. The frame size was 1024 × 1024 pixels, and the dwell time was 500 ns/pixel. Ten images were acquired and overlapped using Velox software and the DCFI (drift correction frame integration) function to increase the signal-to-noise ratio.

The STEM-HAADF images were analyzed using a custom-made Python code framework. The change in lattice distance between different atomic columns was detected by performing peak finding on the output of a fully convolutional neural network that predicts the atomic position as Gaussians in a segmentation map.

The percentage change between Cr and S/Br columns was calculated by $\Delta b = \frac{x - b_{\mathrm{mean}}/2}{b_{\mathrm{mean}}/2}$ where x is the analyzed distance between two atomic positions, and $b_{\mathrm{mean}}/2$ is the mean interatomic column value. The value was obtained from a 6L CrSBr that was used as a reference and extracted by fitting a histogram of interatomic column distances with a normal distribution.

Many-Body Perturbation Theory: *GW*+BSE. CrSBr exhibits spin−orbit coupling and in-plane ferromagnetism. To calculate its electronic ground state from first principles, we employed density functional theory (DFT) in the generalized gradient approximation (GGA).[62] The correct spin structure was provided by the noncollinear DFT formalism.[63,64] This provided the wave function as spinors and is a good starting point for many-body perturbation theory, which also readily includes all effects of noncollinear magnetism.

We calculated the quasiparticle (QP) band structures by including the self-energy $\Sigma(E)$ in the *GW* approximation.[65] Here, the one-particle Green's function G and the screened Coulomb interaction W (including the dielectric response in random phase approximation) are derived, and $\Sigma = iGW$ replaces the DFT exchange correlation energy V_{xc}. The Hamiltonian becomes

$$H^{\mathrm{QP}} = H^{\mathrm{DFT}} + iGW - V_{\mathrm{xc}} \tag{2}$$

where the resulting difference is the quasiparticle correction Δ^{QP} from many-body perturbation theory. The QP band structure energies are then given by

https://doi.org/10.1021/acsnano.2c07316
ACS Nano 2023, 17, 5316−5328

$$E_{n\mathbf{k}}^{\mathrm{QP}} = E_{n\mathbf{k}}^{\mathrm{DFT}} + \langle \psi_{n\mathbf{k}}^{\mathrm{DFT}} | \Sigma(E_{n\mathbf{k}}^{\mathrm{QP}}) - V_{\mathrm{xc}} | \psi_{n\mathbf{k}}^{\mathrm{DFT}} \rangle \quad (3)$$

While the one-shot *GW* is often evaluated only when accounting for the diagonal terms of Σ (and Δ^{QP}, respectively), this is not sufficient for CrSBr (see e.g., refs 66−68). Therefore, we calculate the QP wave functions as a linear combination of the DFT wave functions

$$\psi_{m\mathbf{k}}^{\mathrm{QP}} = \sum_{n} D_{m\mathbf{k}}^{n} \psi_{n\mathbf{k}}^{\mathrm{DFT}} \quad (4)$$

where the coefficients $D_{m\mathbf{k}}^{n}$ are given by the solution of the full eigenvalue problem

$$\sum_{n'} H_{nn'}^{\mathrm{QP}}(\mathbf{k}; E_{m\mathbf{k}}^{\mathrm{QP}}) D_{m\mathbf{k}}^{n'} = E_{m\mathbf{k}}^{\mathrm{QP}} D_{m\mathbf{k}}^{n} \quad (5)$$

For further details see ref 68. Because of the large changes of the band gap, we used a scissor operator to anticipate its opening and, thus, accelerated the self-consistent determination of QP shifts. For the monolayer, bilayer, and bulk, we employed 1.4, 1.1, and 1.0 eV, respectively.

In *GW* we represented all the two-point functions (P, ϵ, W) by a hybrid basis set of Gaussian orbitals with decay constants ranging from 0.14 to 5.1 a_{B}^{2} and plane waves with an energy cutoff set to 1.5 Ry. We applied a k-point sampling of 17 × 13 × 1 points in the first Brillouin zone. For the BSE, we increased the sampling to 32 × 24 × 1 points. For the resulting spectra (Figure 4a,b), an artificial broadening of 35 meV was applied.

Macroscopic Momentum-Dependent Dielectric Function. To obtain the nonlocal macroscopic dielectric function in Figure 4, we calculated the head element of the dielectric matrix in the static limit $\epsilon^{2\mathrm{d}}(\mathbf{q}) := \epsilon_{\mathrm{G}=0,\mathrm{G}'=0}(\mathbf{q})$ using BerkeleyGW[69,70] with 2D Coulomb truncation.[71] To this end, spin-polarized density functional theory (DFT) calculations were carried out using QUANTUM ESPRESSO.[72,73] We applied the generalized gradient approximation (GGA) by Perdew, Burke, and Ernzerhof (PBE)[74,75] and used the optimized norm-conserving Vanderbilt pseudopotential[76] at a plane-wave cutoff of 80 Ry. Uniform meshes with 24 × 18 × 1 k-points were combined with a Fermi−Dirac smearing of 5 mRy. A large vacuum of 28 Å with a truncated Coulomb interaction[77] was included between repeated supercells in the c axis direction. The calculations were performed using the same lattice structure and band gap as in the electronic ground-state calculation for our *GW* approach.

Charge Density Calculations. The charge density calculations shown in Figure 1g,h were performed using the PWmat package. The SG15 pseudopotential and HSE exchange correlation functional were used. A plane-wave energy for the basis set was cut off up to 50 Ry. The charge density shown includes the states in the range of 0.1 eV below the top of the valence band and 0.1 eV above the bottom of the conduction band.

ASSOCIATED CONTENT

Data Availability Statement

The codes used for data analysis as well as *ab initio* calculations are available from the corresponding author on reasonable request. The content of this manuscript is available as an online preprint version (DOI: 10.48550/arXiv.2205.13456).

Supporting Information

The Supporting Information is available free of charge at https://pubs.acs.org/doi/10.1021/acsnano.2c07316.

Three-band $k \times p$ model, monolayer and bulk anisotropic dielectric function of CrSBr, STEM-HAADF of bulk to monolayer CrSBr, Raman spectra of CrOCl, Raman selection rules, laser-excitation power dependence for different thicknesses, power-dependent exciton red shift, photoluminescence excitation spectroscopy of the 1s exciton, oscillations in the photoluminescence signal of the 1s exciton, one-dimensional correlated phases, and interaction effects (charge density wave and stripe crystal) (PDF)

AUTHOR INFORMATION

Corresponding Authors

Julian Klein − *Department of Materials Science and Engineering, Massachusetts Institute of Technology, Cambridge, Massachusetts 02139, United States;* orcid.org/0000-0002-0873-8224; Email: jpklein@mit.edu

Prineha Narang − *College of Letters and Science, UCLA, Los Angeles, California 90095, United States; John A. Paulson School of Engineering and Applied Sciences, Harvard University, Cambridge, Massachusetts 02138, United States;* orcid.org/0000-0003-3956-4594; Email: prineha@ucla.edu

Marko Lončar − *John A. Paulson School of Engineering and Applied Sciences, Harvard University, Cambridge, Massachusetts 02138, United States*; Email: loncar@seas.harvard.edu

Frances M. Ross − *Department of Materials Science and Engineering, Massachusetts Institute of Technology, Cambridge, Massachusetts 02139, United States;* orcid.org/0000-0003-0838-9770; Email: fmross@mit.edu

Authors

Benjamin Pingault − *John A. Paulson School of Engineering and Applied Sciences, Harvard University, Cambridge, Massachusetts 02138, United States; QuTech, Delft University of Technology, 2600 GA Delft, The Netherlands*

Matthias Florian − *Department of Electrical and Computer Engineering, Department of Physics, University of Michigan, Ann Arbor, Michigan 48109, United States*

Marie-Christin Heißenbüttel − *Institut für Festkörpertheorie, Westfälische Wilhelms-Universität Münster, 48149 Münster, Germany;* orcid.org/0000-0002-0580-3713

Alexander Steinhoff − *Institut für Theoretische Physik, Universität Bremen, 28334 Bremen, Germany; Bremen Center for Computational Materials Science, University of Bremen, 28359 Bremen, Germany*

Zhigang Song − *John A. Paulson School of Engineering and Applied Sciences, Harvard University, Cambridge, Massachusetts 02138, United States*

Kierstin Torres − *Department of Materials Science and Engineering, Massachusetts Institute of Technology, Cambridge, Massachusetts 02139, United States;* orcid.org/0000-0002-0463-7805

Florian Dirnberger − *Department of Physics, City College of New York, New York, New York 10031, United States*

Jonathan B. Curtis − *College of Letters and Science, UCLA, Los Angeles, California 90095, United States; John A. Paulson School of Engineering and Applied Sciences, Harvard University, Cambridge, Massachusetts 02138, United States*

Mads Weile − *Center for Visualizing Catalytic Processes (VISION), Department of Physics, Technical University of Denmark, DK-2800 Lyngby, Denmark;* orcid.org/0000-0001-9822-5942

Aubrey Penn − *MIT.nano, Massachusetts Institute of Technology, Cambridge, Massachusetts 02139, United States;* orcid.org/0000-0001-7586-1655

https://doi.org/10.1021/acsnano.2c07316
ACS Nano 2023, 17, 5316−5328

Thorsten Deilmann − *Institut für Festkörpertheorie, Westfälische Wilhelms-Universität Münster, 48149 Münster, Germany*
Rami Dana − *Department of Materials Science and Engineering, Massachusetts Institute of Technology, Cambridge, Massachusetts 02139, United States*
Rezlind Bushati − *Department of Physics, City College of New York, New York, New York 10031, United States; Department of Physics, The Graduate Center, City University of New York, New York, New York 10016, United States*
Jiamin Quan − *Photonics Initiative, CUNY Advanced Science Research Center, New York, New York 10031, United States; Physics Program, Graduate Center, City University of New York, New York, New York 10026, United States*
Jan Luxa − *Department of Inorganic Chemistry, University of Chemistry and Technology Prague, 166 28 Prague 6, Czech Republic*
Zdeněk Sofer − *Department of Inorganic Chemistry, University of Chemistry and Technology Prague, 166 28 Prague 6, Czech Republic*
Andrea Alù − *Photonics Initiative, CUNY Advanced Science Research Center, New York, New York 10031, United States; Physics Program, Graduate Center, City University of New York, New York, New York 10026, United States*
Vinod M. Menon − *Department of Physics, City College of New York, New York, New York 10031, United States; Department of Physics, The Graduate Center, City University of New York, New York, New York 10016, United States;* orcid.org/0000-0002-9725-6445
Ursula Wurstbauer − *Institute of Physics and Center for Nanotechnology, University of Münster, 48149 Münster, Germany*
Michael Rohlfing − *Institut für Festkörpertheorie, Westfälische Wilhelms-Universität Münster, 48149 Münster, Germany*

Complete contact information is available at: https://pubs.acs.org/10.1021/acsnano.2c07316

Author Contributions

J.K. and F.M.R. conceived the project and designed the experiments; J.K. and K.T. prepared the samples; J.K. and A.P. collected STEM data; J.K. and B.P. performed PL and PLE optical measurements; J.K. and K.T. performed polarization resolved Raman measurements; F.D., R.B., and J.Q. performed magneto-reflectivity measurements; R.D. and J.K. performed STM/STS measurements; Z.Sofer and J.L. synthesized high-quality CrSBr crystals; M.F., M.-C.H., A.S., T.D., and M.R. provided DFT+*GW* and BSE calculations; J.K. and M.W. analyzed the experimental data; Z.Song, provided charge density calculations with input from P.N. and, furthermore, provided the $k \times p$ model; J.B.C. provided additional theoretical insights into the correlated physics; M.L., U.W., V.M.M., and A.A. discussed results; and J.K. wrote the manuscript with input from all coauthors.

Notes

The authors declare no competing financial interest.

ACKNOWLEDGMENTS

J.K. and M.F. acknowledge support by the Alexander von Humboldt foundation. B.P. is a Marie Skłodowska-Curie fellow and acknowledges funding from the European Union's Horizon 2020 research and innovation programme under the Grant Agreement No. 840968 (COHESiV). F.M.R. acknowledges funding from the U.S. Department of Energy, Office of Basic Energy Sciences, Division of Materials Sciences and Engineering under Award DE-SC0019336 for STEM characterization. Work by J.B.C. and P.N. is partially supported by the Quantum Science Center (QSC), a National Quantum Information Science Research Center of the U.S. Department of Energy (DOE). J.B.C. is an HQI Prize Postdoctoral Fellow and gratefully acknowledges support from the Harvard Quantum Initiative. Z.Song is supported through the Department of Energy BES QIS program on 'van der Waals Reprogrammable Quantum Simulator' under award number DE-SC0022277 for the work on long-range correlations, as well as partially supported by the Quantum Science Center (QSC), a National Quantum Information Science Research Center of the U.S. Department of Energy (DOE) on probing quantum matter. P.N. acknowledges support as a Moore Inventor Fellow through Grant No. GBMF8048 and gratefully acknowledges support from the Gordon and Betty Moore Foundation, as well as support from a NSF CAREER Award under Grant No. NSF-ECCS-1944085. M.F. and A.S. were supported through a grant for CPU time at the HLRN (Berlin/Göttingen). M.W. is supported by the Center for Visualizing Catalytic Processes sponsored by the Danish National Research Foundation (DNRF146). Z.Sofer was supported by ERC-CZ program (project LL2101) from Ministry of Education Youth and Sports (MEYS). The optical PL and PLE spectroscopy work at low temperatures was supported by ARO MURI (Grant No. W911NF1810432), HEADS-QON (Grant No. DE-SC0020376), ONR MURI (Grant No. N00014-15-1-2761), CIQM (Grant No. DMR-1231319), and ONR (Grant No. N00014-20-1-2425). Work at CCNY was supported through the NSF QII TAQS 1936276 (V.M.M.) and the DARPA Nascent Light Matter program (R.B.). F.D. was funded by the Deutsche Forschungsgemeinschaft (DFG, German Research Foundation) through Projektnummer 451072703. M.-C.H., T.D., and M.R. gratefully acknowledge the financial support from German Research Foundation (DFG Project No. DE 2749/2-1), the DFG Collaborative Research Center SFB 1083 (Project No. A13), and computing time granted by the John von Neumann Institute for Computing (NIC) and provided on the supercomputer JUWELS at Jülich Supercomputing Centre (JSC). A.A. and J.Q. acknowledge support from a Vannevar Bush Faculty Fellowship, the AFOSR DURIP and MURI programs, and the Simons Foundation. This work was carried out in part through the use of MIT.nano's facilities.

REFERENCES

(1) Paredes, B.; Widera, A.; Murg, V.; Mandel, O.; Folling, S.; Cirac, I.; Shlyapnikov, G. V.; Hansch, T. W.; Bloch, I. Tonks−Girardeau gas of ultracold atoms in an optical lattice. *Nature* **2004**, *429*, 277−281.
(2) Blumenstein, C.; Schafer, J.; Mietke, S.; Meyer, S.; Dollinger, A.; Lochner, M.; Cui, X. Y.; Patthey, L.; Matzdorf, R.; Claessen, R. Atomically controlled quantum chains hosting a Tomonaga−Luttinger liquid. *Nat. Phys.* **2011**, *7*, 776−780.
(3) Rao, A. M.; Richter, E.; Bandow, S.; Chase, B.; Eklund, P. C.; Williams, K. A.; Fang, S.; Subbaswamy, K. R.; Menon, M.; Thess, A.; Smalley, R. E.; Dresselhaus, G.; Dresselhaus, M. S. Diameter-selective Raman scattering from vibrational modes in carbon nanotubes. *Science* **1997**, *275*, 187−191.
(4) Saito, R.; Takeya, T.; Kimura, T.; Dresselhaus, G.; Dresselhaus, M. S. Raman intensity of single-wall carbon nanotubes. *Phys. Rev. B* **1998**, *57*, 4145−4153.

(5) Bockrath, M.; Cobden, D. H.; Lu, J.; Rinzler, A. G.; Smalley, R. E.; Balents, L.; McEuen, P. L. Luttinger-liquid behaviour in carbon nanotubes. *Nature* **1999**, *397*, 598−601.
(6) Brown, S. D. M.; Jorio, A.; Corio, P.; Dresselhaus, M. S.; Dresselhaus, G.; Saito, R.; Kneipp, K. Origin of the Breit-Wigner-Fano lineshape of the tangential G-band feature of metallic carbon nanotubes. *Phys. Rev. B* **2001**, *63*, 155414.
(7) Nguyen, K. T.; Gaur, A.; Shim, M. Fano lineshape and phonon softening in single isolated metallic carbon nanotubes. *Phys. Rev. Lett.* **2007**, *98*, 145504.
(8) Farhat, H.; Son, H.; Samsonidze, G. G; Reich, S.; Dresselhaus, M. S.; Kong, J. Phonon softening in individual metallic carbon nanotubes due to the Kohn anomaly. *Phys. Rev. Lett.* **2007**, *99*, 145506.
(9) Lake, B.; Tennant, D. A.; Frost, C. D.; Nagler, S. E. Quantum criticality and universal scaling of a quantum antiferromagnet. *Nat. Mater.* **2005**, *4*, 329−334.
(10) Langer, L.; Bayot, V.; Grivei, E.; Issi, J.-P.; Heremans, J. P.; Olk, C. H.; Stockman, L.; Van Haesendonck, C.; Bruynseraede, Y. Quantum transport in a multiwalled carbon nanotube. *Phys. Rev. Lett.* **1996**, *76*, 479−482.
(11) Balandin, A. A.; Kargar, F.; Salguero, T. T.; Lake, R. K. One-dimensional van der Waals quantum materials. *Mater. Today* **2022**, *55*, 74−91.
(12) Remskar, M.; Mrzel, A.; Skraba, Z.; Jesih, A.; Ceh, M.; Demsar, J.; Stadelmann, P.; Levy, F.; Mihailovic, D. Self-assembly of subnanometer-diameter single-wall MoS_2 nanotubes. *Science* **2001**, *292*, 479−481.
(13) Golberg, D.; Bando, Y.; Tang, C.; Zhi, C. Boron nitride nanotubes. *Adv. Mater.* **2007**, *19*, 2413−2432.
(14) Pfeiffer, L.; Stormer, H.L.; Baldwin, K.W.; West, K.W.; Goni, A.R.; Pinczuk, A.; Ashoori, R.C.; Dignam, M.M.; Wegscheider, W. Cleaved edge overgrowth for quantum wire fabrication. *J. Cryst. Growth* **1993**, *127*, 849−857.
(15) Meier, S.; Faria Junior, P. E.; Haas, F.; Heller, E.-S.; Dirnberger, F.; Zeller, V.; Korn, T.; Fabian, J.; Bougeard, D.; Schüller, C. Intersubband excitations in ultrathin core-shell nanowires in the one-dimensional quantum limit probed by resonant inelastic light scattering. *Phys. Rev. B* **2021**, *104*, 235307.
(16) Felser, C.; Finckh, E. W.; Kleinke, H.; Rocker, F.; Tremel, W. Electronic properties of $ZrTe_3$. *J. Mater. Chem.* **1998**, *8*, 1787−1798.
(17) Meerschaut, A.; Rouxel, J. Pseudo-one-dimensional MX3 and MX4 transition metal chalcogenides. In *Crystal Chemistry and Properties of Materials with Quasi-One-Dimensional Structures*; Springer Netherlands, 1986; pp 205−279.
(18) Jin, Y.; Li, X.; Yang, J. Single layer of MX_3 (M = Ti, Zr; X = S, Se, Te): a new platform for nano-electronics and optics. *Phys. Chem. Chem. Phys.* **2015**, *17*, 18665−18669.
(19) Deshpande, V. V.; Bockrath, M.; Glazman, L. I.; Yacoby, A. Electron liquids and solids in one dimension. *Nature* **2010**, *464*, 209−216.
(20) Furdyna, J. K. Diluted magnetic semiconductors. *J. Appl. Phys.* **1988**, *64*, R29−R64.
(21) Wurstbauer, U.; Śliwa, C.; Weiss, D.; Dietl, T.; Wegscheider, W. Hysteretic magnetoresistance and thermal bistability in a magnetic two-dimensional hole system. *Nat. Phys.* **2010**, *6*, 955−959.
(22) Gong, C.; Li, L.; Li, Z.; Ji, H.; Stern, A.; Xia, Y.; Cao, T.; Bao, W.; Wang, C.; Wang, Y.; Qiu, Z. Q.; Cava, R. J.; Louie, S. G.; Xia, J.; Zhang, X. Discovery of intrinsic ferromagnetism in two-dimensional van der Waals crystals. *Nature* **2017**, *546*, 265−269.
(23) Huang, B.; Clark, G.; Navarro-Moratalla, E.; Klein, D. R.; Cheng, R.; Seyler, K. L.; Zhong, D.; Schmidgall, E.; McGuire, M. A.; Cobden, D. H.; Yao, W.; Xiao, D.; Jarillo-Herrero, P.; Xu, X. Layer-dependent ferromagnetism in a van der Waals crystal down to the monolayer limit. *Nature* **2017**, *546*, 270−273.
(24) Shaz, M.; van Smaalen, S.; Palatinus, L.; Hoinkis, M.; Klemm, M.; Horn, S.; Claessen, R. Spin-Peierls transition in TiOCl. *Phys. Rev. B* **2005**, *71*, 100405.
(25) Blanco-Canosa, S.; Rivadulla, F.; Pineiro, A.; Pardo, V.; Baldomir, D.; Khomskii, D. I.; Abd-Elmeguid, M. M.; Lopez-Quintela, M. A.; Rivas, J. Enhanced dimerization of TiOCl under pressure: Spin-Peierls to Peierls transition. *Phys. Rev. Lett.* **2009**, *102*, 056406.
(26) Prodi, A.; Helton, J. S.; Feng, Y.; Lee, Y. S. Pressure-induced spin-Peierls to incommensurate charge-density-wave transition in the ground state of TiOCl. *Phys. Rev. B* **2010**, *81*, No. 201103.
(27) Katscher, H.; Hahn, H. Über Chalkogenidhalogenide des dreiwertigen Chroms. *Die Naturwissenschaften* **1966**, *53*, 361−361.
(28) Göser, O.; Paul, W.; Kahle, H. Magnetic properties of CrSBr. *J. Magn. Magn. Mater.* **1990**, *92*, 129−136.
(29) Wang, C.; Zhou, X.; Zhou, L.; Tong, N.-H.; Lu, Z.-Y.; Ji, W. A family of high-temperature ferromagnetic monolayers with locked spin-dichroism-mobility anisotropy: MnNX and CrCX (X = Cl, Br, I; C = S, Se, Te). *Science Bulletin* **2019**, *64*, 293−300.
(30) Wang, H.; Qi, J.; Qian, X. Electrically tunable high curie temperature two-dimensional ferromagnetism in van der Waals layered crystals. *Appl. Phys. Lett.* **2020**, *117*, 083102.
(31) Telford, E. J.; Dismukes, A. H.; Lee, K.; Cheng, M.; Wieteska, A.; Bartholomew, A. K.; Chen, Y.-S.; Xu, X.; Pasupathy, A. N.; Zhu, X.; Dean, C. R.; Roy, X. Layered antiferromagnetism induces large negative magnetoresistance in the van der Waals semiconductor CrSBr. *Adv. Mater.* **2020**, *32*, 2003240.
(32) Lee, K.; Dismukes, A. H.; Telford, E. J.; Wiscons, R. A.; Wang, J.; Xu, X.; Nuckolls, C.; Dean, C. R.; Roy, X.; Zhu, X. Magnetic order and symmetry in the 2D semiconductor CrSBr. *Nano Lett.* **2021**, *21*, 3511−3517.
(33) Wilson, N. P.; Lee, K.; Cenker, J.; Xie, K.; Dismukes, A. H.; Telford, E. J.; Fonseca, J.; Sivakumar, S.; Dean, C.; Cao, T.; Roy, X.; Xu, X.; Zhu, X. Interlayer electronic coupling on demand in a 2D magnetic semiconductor. *Nat. Mater.* **2021**, *20*, 1657−1662.
(34) Yang, K.; Wang, G.; Liu, L.; Lu, D.; Wu, H. Triaxial magnetic anisotropy in the two-dimensional ferromagnetic semiconductor CrSBr. *Phys. Rev. B* **2021**, *104*, 144416.
(35) Klein, J.; Pham, T.; Thomsen, J. D.; Curtis, J. B.; Denneulin, T.; Lorke, M.; Florian, M.; Steinhoff, A.; Wiscons, R. A.; Luxa, J.; Sofer, Z.; Jahnke, F.; Narang, P.; Ross, F. M. Control of structure and spin texture in the van der Waals layered magnet CrSBr. *Nat. Commun.* **2022**, *13*, 5420.
(36) Klein, J.; Song, Z.; Pingault, B.; Dirnberger, F.; Chi, H.; Curtis, J. B.; Dana, R.; Bushati, R.; Quan, J.; Dekanovsky, L.; Sofer, Z.; Alu, A.; Menon, V. M.; Moodera, J. S.; Loncar, M.; Narang, P.; Ross, F. M. Sensing the local magnetic environment through optically active defects in a layered magnetic semiconductor. *ACS Nano* **2023**, *17*, 288−299.
(37) Telford, E. J.; Dismukes, A. H.; Dudley, R. L.; Wiscons, R. A.; Lee, K.; Chica, D. G.; Ziebel, M. E.; Han, M.-G.; Yu, J.; Shabani, S.; Scheie, A.; Watanabe, K.; Taniguchi, T.; Xiao, D.; Zhu, Y.; Pasupathy, A. N.; Nuckolls, C.; Zhu, X.; Dean, C. R.; Roy, X. Coupling between magnetic order and charge transport in a two-dimensional magnetic semiconductor. *Nat. Mater.* **2022**, *21*, 754−760.
(38) Wu, F.; Gutierrez-Lezama, I.; Lopez-Paz, S. A.; Gibertini, M.; Watanabe, K.; Taniguchi, T.; von Rohr, F. O.; Ubrig, N.; Morpurgo, A. F. Quasi-1D electronic transport in a 2D magnetic semiconductor. *Adv. Mater.* **2022**, *34*, 2109759.
(39) Torres, K.; Kuc, A.; Maschio, L.; Pham, T.; Reidy, K.; Dekanovsky, L.; Sofer, Z.; Ross, F. M.; Klein, J. Probing defects and spin-phonon coupling in CrSBr via resonant Raman scattering. *Adv. Funct. Mater.* **2023**, 2211366.
(40) Bae, Y. J.; Wang, J.; Scheie, A.; Xu, J.; Chica, D. G.; Diederich, G. M.; Cenker, J.; Ziebel, M. E.; Bai, Y.; Ren, H.; Dean, C. R.; Delor, M.; Xu, X.; Roy, X.; Kent, A. D.; Zhu, X. Exciton-coupled coherent magnons in a 2D semiconductor. *Nature* **2022**, *609*, 282−286.
(41) Tran, V.; Yang, L. Scaling laws for the band gap and optical response of phosphorene nanoribbons. *Phys. Rev. B* **2014**, *89*, 245407.
(42) Mak, K. F.; Lee, C.; Hone, J.; Shan, J.; Heinz, T. F. Atomically thin $MoSe_2$: A new direct-gap semiconductor. *Phys. Rev. Lett.* **2010**, *105*, 136805.

https://doi.org/10.1021/acsnano.2c07316
ACS Nano 2023, 17, 5316−5328

(43) Splendiani, A.; Sun, L.; Zhang, Y.; Li, T.; Kim, J.; Chim, C.-Y.; Galli, G.; Wang, F. Emerging photoluminescence in monolayer MoS_2. *Nano Lett.* **2010**, *10*, 1271−1275.
(44) Cadiz, F.; Courtade, E.; Robert, C.; Wang, G.; Shen, Y.; Cai, H.; Taniguchi, T.; Watanabe, K.; Carrere, H.; Lagarde, D.; Manca, M.; Amand, T.; Renucci, P.; Tongay, S.; Marie, X.; Urbaszek, B. Excitonic linewidth approaching the homogeneous limit in MoS_2-based van der Waals heterostructures. *Physical Review X* **2017**, *7*, 021026.
(45) Shree, S.; Semina, M.; Robert, C.; Han, B.; Amand, T.; Balocchi, A.; Manca, M.; Courtade, E.; Marie, X.; Taniguchi, T.; Watanabe, K.; Glazov, M. M.; Urbaszek, B. Observation of exciton-phonon coupling in $MoSe_2$ monolayers. *Phys. Rev. B* **2018**, *98*, 035302.
(46) Spijkerman, A.; de Boer, J. L.; Meetsma, A.; Wiegers, G. A.; van Smaalen, S. X-ray crystal-structure refinement of the nearly commensurate phase of 1T-TaS_2 in (3 + 2)-dimensional superspace. *Phys. Rev. B* **1997**, *56*, 13757−13767.
(47) Johannes, M. D.; Mazin, I. I. Fermi surface nesting and the origin of charge density waves in metals. *Phys. Rev. B* **2008**, *77*, 165135.
(48) Hayes, W.; Loudon, R. *Scattering of light by crystals*; Wiley: New York, NY, 1978.
(49) Zhang, T.; Wang, Y.; Li, H.; Zhong, F.; Shi, J.; Wu, M.; Sun, Z.; Shen, W.; Wei, B.; Hu, W.; Liu, X.; Huang, L.; Hu, C.; Wang, Z.; Jiang, C.; Yang, S.; Zhang, Q.-m.; Qu, Z. Magnetism and optical anisotropy in van der Waals antiferromagnetic insulator CrOCl. *ACS Nano* **2019**, *13*, 11353−11362.
(50) Zhang, J.; Peng, Z.; Soni, A.; Zhao, Y.; Xiong, Y.; Peng, B.; Wang, J.; Dresselhaus, M. S.; Xiong, Q. Raman spectroscopy of few-quintuple layer topological insulator Bi_2Se_3 nanoplatelets. *Nano Lett.* **2011**, *11*, 2407−2414.
(51) Tan, Q.-H.; Sun, Y.-J.; Liu, X.-L.; Zhao, Y.; Xiong, Q.; Tan, P.-H.; Zhang, J. Observation of forbidden phonons, Fano resonance and dark excitons by resonance Raman scattering in few-layer WS_2. *2D Materials* **2017**, *4*, 031007.
(52) Caimi, G.; Degiorgi, L.; Kovaleva, N. N.; Lemmens, P.; Chou, F. C. Infrared optical properties of the spin-1/2 quantum magnet TiOCl. *Phys. Rev. B* **2004**, *69*, 125108.
(53) Dirnberger, F.; Quan, J.; Bushati, R.; Diederich, G.; Florian, M.; Klein, J.; Mosina, K.; Sofer, Z.; Xu, X; Kamra, A.; García-Vidal, F. J.; Alù, A.; Menon, V. M. Cavity-controlled magneto-optical properties of a strongly coupled van der Waals magnet. *arXiv*, January 18, 2023, 2301.07593, ver. *1*. DOI: 10.48550/arXiv.2301.07593.
(54) Steinhoff, A.; Rösner, M.; Jahnke, F.; Wehling, T. O.; Gies, C. Influence of excited carriers on the optical and electronic properties of MoS_2. *Nano Lett.* **2014**, *14*, 3743−3748.
(55) Chow, C. M.; Yu, H.; Jones, A. M.; Schaibley, J. R.; Koehler, M.; Mandrus, D. G.; Merlin, R.; Yao, W.; Xu, X. Phonon-assisted oscillatory exciton dynamics in monolayer $MoSe_2$. *npj 2D Materials and Applications* **2017**, *1*, 33.
(56) Hwangbo, K.; Zhang, Q.; Jiang, Q.; Wang, Y.; Fonseca, J.; Wang, C.; Diederich, G. M.; Gamelin, D. R.; Xiao, D.; Chu, J.-H.; Yao, W.; Xu, X. Highly anisotropic excitons and multiple phonon bound states in a van der Waals antiferromagnetic insulator. *Nat. Nanotechnol.* **2021**, *16*, 655−660.
(57) Ergecen, E.; Ilyas, B.; Mao, D.; Po, H. C.; Yilmaz, M. B.; Kim, J.; Park, J.-G.; Senthil, T.; Gedik, N. Magnetically brightened dark electron-phonon bound states in a van der waals antiferromagnet. *Nat. Commun.* **2022**, *13*, 98.
(58) Toyozawa, Y.; Hermanson, J. Exciton-phonon bound state: A new quasiparticle. *Phys. Rev. Lett.* **1968**, *21*, 1637−1641.
(59) Schulz, H. Wigner crystal in one dimension. *Phys. Rev. Lett.* **1993**, *71*, 1864.
(60) Spivak, B.; Kivelson, S. A. Phases intermediate between a two-dimensional electron liquid and Wigner crystal. *Phys. Rev. B* **2004**, *70*, 155114.
(61) Emery, V. J.; Fradkin, E.; Kivelson, S. A.; Lubensky, T. C. Quantum theory of the smectic metal state in stripe phases. *Phys. Rev. Lett.* **2000**, *85*, 2160−2163.
(62) Perdew, J. P.; Chevary, J. A.; Vosko, S. H.; Jackson, K. A.; Pederson, M. R.; Singh, D. J.; Fiolhais, C. Atoms, molecules, solids, and surfaces: Applications of the generalized gradient approximation for exchange and correlation. *Phys. Rev. B* **1992**, *46*, 6671−6687.
(63) Stärk, B.; Krüger, P.; Pollmann, J. Magnetic anisotropy of thin Co and Ni films on diamond surfaces. *Phys. Rev. B* **2011**, *84*, 195316.
(64) Sandratskii, L. M. Noncollinear magnetism in itinerant-electron systems: Theory and applications. *Adv. Phys.* **1998**, *47*, 91−160.
(65) Hedin, L. New Method for Calculating the One-Particle Green's Function with Application to the Electron-Gas Problem. *Phys. Rev.* **1965**, *139*, A796−A823.
(66) Deilmann, T. Valley selectivity induced by magnetic adsorbates: Triplet oxygen on monolayer MoS_2. *Phys. Rev. B* **2020**, *101*, 085130.
(67) Förster, T.; Krüger, P.; Rohlfing, M. Two-dimensional topological phases and electronic spectrum of Bi_2Se_3 thin films from *GW* calculations. *Phys. Rev. B* **2015**, *92*, 201404.
(68) Heißenbüttel, M.-C.; Deilmann, T.; Krüger, P.; Rohlfing, M. Valley-dependent interlayer excitons in magnetic WSe_2/CrI_2. *Nano Lett.* **2021**, *21*, 5173−5178.
(69) Hybertsen, M. S.; Louie, S. G. Electron correlation in semiconductors and insulators: Band gaps and quasiparticle energies. *Phys. Rev. B* **1986**, *34*, 5390−5413.
(70) Deslippe, J.; Samsonidze, G.; Strubbe, D. A.; Jain, M.; Cohen, M. L.; Louie, S. G. BerkeleyGW: A massively parallel computer package for the calculation of the quasiparticle and optical properties of materials and nanostructures. *Comput. Phys. Commun.* **2012**, *183*, 1269−1289.
(71) Qiu, D. Y.; da Jornada, F. H.; Louie, S. G. Screening and many-body effects in two-dimensional crystals: Monolayer MoS_2. *Phys. Rev. B* **2016**, *93*, 235435.
(72) Giannozzi, P.; Baroni, S.; Bonini, N.; Calandra, M.; Car, R.; Cavazzoni, C.; Ceresoli, D.; Chiarotti, G. L; Cococcioni, M.; Dabo, I.; Dal Corso, A.; de Gironcoli, S.; Fabris, S.; Fratesi, G.; Gebauer, R.; Gerstmann, U.; Gougoussis, C.; Kokalj, A.; Lazzeri, M.; Martin-Samos, L.; Marzari, N.; Mauri, F.; Mazzarello, R.; Paolini, S.; Pasquarello, A.; Paulatto, L.; Sbraccia, C.; Scandolo, S.; Sclauzero, G.; Seitsonen, A. P; Smogunov, A.; Umari, P.; Wentzcovitch, R. M QUANTUM ESPRESSO: a modular and open-source software project for quantum simulations of materials. *J. Phys.: Condens. Matter* **2009**, *21*, 395502.
(73) Giannozzi, P; Andreussi, O; Brumme, T; Bunau, O; Buongiorno Nardelli, M; Calandra, M; Car, R; Cavazzoni, C; Ceresoli, D; Cococcioni, M; Colonna, N; Carnimeo, I; Dal Corso, A; de Gironcoli, S; Delugas, P; DiStasio, R A; Ferretti, A; Floris, A; Fratesi, G; Fugallo, G; Gebauer, R; Gerstmann, U; Giustino, F; Gorni, T; Jia, J; Kawamura, M; Ko, H-Y; Kokalj, A; Kucukbenli, E; Lazzeri, M; Marsili, M; Marzari, N; Mauri, F; Nguyen, N L; Nguyen, H-V; Otero-de-la-Roza, A; Paulatto, L; Ponce, S; Rocca, D; Sabatini, R; Santra, B; Schlipf, M; Seitsonen, A P; Smogunov, A; Timrov, I; Thonhauser, T; Umari, P; Vast, N; Wu, X; Baroni, S Advanced capabilities for materials modelling with quantum ESPRESSO. *J. Phys.: Condens. Matter* **2017**, *29*, 465901.
(74) Perdew, J. P.; Burke, K.; Ernzerhof, M. Generalized Gradient Approximation Made Simple. *Phys. Rev. Lett.* **1996**, *77*, 3865−3868.
(75) Perdew, J. P.; Burke, K.; Ernzerhof, M. Generalized Gradient Approximation Made Simple [Phys. Rev. Lett. 77, 3865 (1996)]. *Phys. Rev. Lett.* **1997**, *78*, 1396−1396.
(76) van Setten, M.J.; Giantomassi, M.; Bousquet, E.; Verstraete, M.J.; Hamann, D.R.; Gonze, X.; Rignanese, G.-M. The PseudoDojo: Training and grading a 85 element optimized norm-conserving pseudopotential table. *Comput. Phys. Commun.* **2018**, *226*, 39−54.
(77) Sohier, T.; Calandra, M.; Mauri, F. Density functional perturbation theory for gated two-dimensional heterostructures: Theoretical developments and application to flexural phonons in graphene. *Phys. Rev. B* **2017**, *96*, 075448.